Hydrodynamic dispersion at stagnation points: Simulations and experiments

E. G. Flekkøy,[1,*] U. Oxaal,[2] J. Feder,[2] and T. Jøssang[1,2]
[1] *Centre for Advanced Study at The Norwegian Academy of Science and Letters, P.O. Box 7606 Skillebekk, 0205 Oslo, Norway*
[2] *Department of Physics, University of Oslo, P.O. Box 1048 Blindern, 0316 Oslo, Norway*
(Received 14 November 1994; revised manuscript received 4 May 1995)

The spreading of a passive tracer that is convected back and forth inside a porous medium depends both on the random characteristics of the medium and on the presence of stagnation points. We single out the effect of the latter in the present study of hydrodynamic dispersion in the creeping (low Reynolds number) high Péclet number flow around the single stagnation point on a cylindrical obstacle in a Hele-Shaw cell [U. Oxaal, E. G. Flekkøy, and J. Feder, Phys. Rev. Lett. **72**, 3514 (1994)]. Employing both experiments and lattice Boltzmann simulations we analyze the dispersive spreading of a single tracer line, which is initially perpendicular to the flow direction and then convected back and forth around the cylinder. The lattice Boltzmann model used is a modification of the recently introduced two-dimensional lattice Bhatnagar-Gross-Krook model for miscible fluid dynamics [E. G. Flekkøy, Phys. Rev. E **47**, 4247 (1993)]. It includes the full three-dimensional viscous interaction in the Hele-Shaw cell and, in the case of steady state flow, it allows for a freely tunable Reynolds number. The diffusive behavior of the system is explored extensively and excellent agreement between simulations and experiment is observed. A method to determine very small molecular diffusion coefficients D, which relies on the combination of results from experiment and simulation, is proposed. It is demonstrated that there is good agreement between the result of this method and independent measurements that are carried out in the present case of relatively large D values.

PACS number(s): 47.10.+g, 02.70.−c, 51.10.+y

I. INTRODUCTION

A tracer in a moving fluid is transported under the combined action of molecular diffusion and convection, i.e., it is dispersed. Here we study the dispersion that arises when the tracer is convected back and forth once by reversal of the flow direction. When the Reynolds number is sufficiently small, the velocity field will be reversible so that, in the absence of molecular diffusion, the tracer particles would be transported back to their original position. Depending on the local flow velocity and the molecular diffusion constant D, one or the other of the two mechanisms may dominate. Variations in the velocity field may, as in the present case, result in transport that is diffusion dominated in some regions and convection dominated in others. In regions where the velocity becomes very small, the transport, if any, will be dominated by diffusion. Correspondingly, in such regions a diffusive displacement of a tracer particle will correspond to a relatively large difference in the convective transport time, i.e., the time it takes for a particle that is convected with the flow to reach a given point. When the flow direction is reversed, this will cause the convection to bring the particles far apart and a large dispersive spread in the returned concentration profile results. Hence, even if the integrated convective transport vanishes, it greatly enhances the resulting dispersion. A particularly simple system where this effect can be studied is that of a single stagnation point. At stagnation points, where the flow velocity is directed toward the wall at arbitrarily small distances, convection decays and diffusion takes over relatively rapidly. *Stagnation point dispersion*, which is the subject of this paper, is caused by the presence of stagnation points alone and can be studied even in very simple geometries.

Geometric dispersion in a porous medium, on the other hand, is dominated by the rapidly varying flow field induced by the random medium: Streamlines that pass through the medium along different paths might at some points come close to each other. Hence, even when stagnant zones play no role, the differences in the convective transport times between adjacent streamlines might be very large and produce a corresponding spread in the tracer concentration profile on return of the flow. The dispersion of tracers that are convected back and forth in a porous medium [3] and fractures [4] has been studied with the focus on the effects of geometric dispersion.

The above description refers to the special cases where the flow is reversed and the overall convective transport vanishes. The resulting dispersion may be called *echo* dispersion. Experiments on dispersion in porous media [5,6] have mostly concentrated on measuring the average effects of many stagnation points in the case where the flow direction is *not* reversed, as have analytic studies of stagnation point dispersion in porous media [7]. When the Péclet number Pe is not too small the dispersion is then mostly caused by velocity differences, i.e., by variations in the convective transport, and would also arise

*Current address: PMMH, Ecole Supérieure de Physique et Chimie Industrielle, 10 rue Vauquelin, 75005 Paris, France.

if diffusion were absent ($D = 0$). In the case of flow in random media the (coarsegrained) dispersion may be characterized by a longitudinal dispersion coefficient $D_{\|}$, which is proportional to the mean flow velocity and depends strongly on the geometric characteristics of the medium. Numerical work in this context has been carried out to determine the distribution of the convective transport times for tracers convected past a sphere and to estimate the amount of tracer that is caught in the stagnant region close to the stagnation point [8]. This result was then applied to determine a correction term to $D_{\|}$ of the form $\ln \mathrm{Pe}$.

The aim of the present work is twofold. The first point of interest is to describe the detailed dynamics and structure of stagnation point dispersion in a simple geometry and its potential applications. The second point of interest is to verify the physical behavior of the tool with which we study it, i.e., the lattice Boltzmann model for miscible fluid dynamics [2]. This model belongs to a general class of models [9,10] that have evolved from the lattice gas automata (LGA) model for the Navier-Stokes equation introduced by Frisch, Hasslacher, and Pomeau [11] and it is closely related to the lattice Boltzmann model for miscible fluids introduced by Holme and Rothman [12]. Within this class of models a comparison with experiments has been done for moderate to high Reynolds number flow around a cylinder [13] and for spinodal decomposition in a shear flow [14]. This paper presents a detailed quantitative comparison in which simulations and experiments are mutually adapted in order to verify the algorithmic model and to make the simulations a practical tool for understanding a particular experiment and extending the experimental results.

At the outset we wish to draw attention to the main results, which are shown in Figs. 2(a)–2(c) and 7. Figure 2 shows the qualitative agreement between the concentration profiles obtained from experiment and simulation. Figure 7 shows the corresponding quantitative result. It depicts the effective dispersion coefficient D_{disp} (in units of D), defined as the mean square spread per unit time of the returned profile, for the experiment and simulations, respectively. The agreement is seen to be excellent.

We argue that in the regime of sufficiently high Péclet numbers, where $D_{\mathrm{disp}} \propto D$, the matching of the simulated and experimental results will provide a possible experimental method for determining very small molecular diffusion coefficients. In the simulations both D and D_{disp} are known with good accuracy, whereas in the experiment the larger values of D_{disp} can be measured much more accurately and faster than D. We find good agreement between the experimental value of D thus determined and values from independent measurements.

We describe how the two-dimensional lattice Boltzmann model can be adapted to simulate the (three-dimensional) flow in a Hele-Shaw cell. This adaptation is done much as in Ref. [12] and relies on a simplified description of the viscous interaction with the top and bottom plates of the Hele-Shaw cell. By comparing simulations with known analytic results for flow in a simple rectangular channel it is shown that the flow field in the layer between the top and bottom plates is well described by the model.

In addition to the physical parameters, such as the transport coefficients, the model contains a parameter, known as the G factor, that can be used to tune the Reynolds number of steady state flows at fixed viscosity, flow rate, and system size. This is utilized in the simulations to obtain the same Reynolds number, as in the experiment, and it can be used to explore the regime of higher Reynolds number, which is not available experimentally.

The paper is organized as follows. In Sec. II we describe the experiment that motivates the development and description of the model in Sec. III, where we perform preliminary tests of the model for the case of flow in a channel without obstacles and stagnation points. Sections IV and V contain a comparison between experiment and simulations as well as a corresponding discussion of the quantities used for this comparison.

II. SYSTEM DESCRIPTION

In the experiment (see Fig. 1) a thin straight filament of dyed fluid is placed in the middle between the top and bottom plates of the Hele-Shaw cell. When the flow is initiated, the filament folds and stretches around the cylindrical obstacle placed in the middle of the channel. In the simulations the concentration field C is initialized with

$$C(\boldsymbol{x},0) = \begin{cases} C_0 \left\{1 - [(x - x_0)/a]^2\right\}^{1/2} \\ \text{where } |x - x_0| < a \\ 0 \\ \text{where } |x - x_0| > a, \end{cases} \tag{1}$$

where a is the initial half-width of the tracer line. This

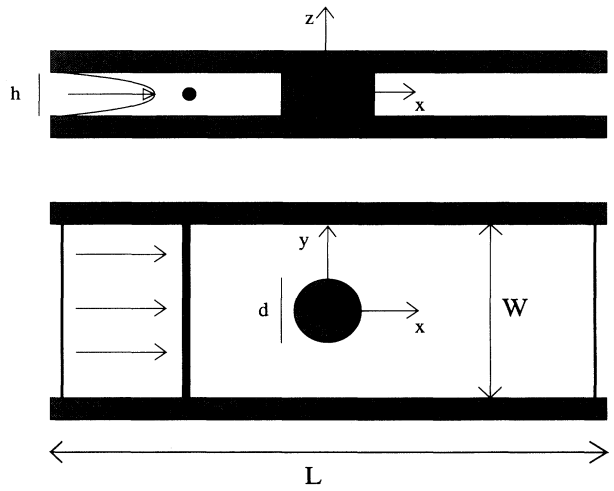

FIG. 1. Hele-Shaw cell with the cylindrical obstacle as seen from the side and from above. The inside measurements of the channel are $30 \times 5 \times 0.9$ cm^3 in the x, y, and z directions, respectively, and the cylinder diameter $d = 2r_0 = 1.05$ cm. The tracer fluid, initially injected as a straight line extending in the y direction, is shown in black. The thickness of the line is slightly exaggerated as compared to the experiment.

concentration profile corresponds to the projection into the xy plane of the cylindrical shaped tracer profile of the experiment. Both in the experiment and the simulations the flow is reversed when the tracer has reached a certain distance $x_{\max}$ past the center of the cylinder. In the absence of thermal convection the line stays in the middle between the top and bottom plates where the flow velocity is at a maximum. The stretching of the line in the vicinity of the stagnation point drastically increases the ratio of the characteristic diffusion length to the local linewidth. In general, where the flow causes the tracer line to stretch, the concentration gradient increases and the spread of the returned profile will be correspondingly larger. Thus the line of dye returns with the characteristic smeared central region. Figures 2(b) (experiment) and 2(c) (simulation) show how the flow maps the diffusive spread that occurs close to the cylinder to the rather large scale structure that is quantified by D_{disp}. We see that the simulations capture the main qualitative features observed in the experiment: The dispersed tracers show the same characteristic spread in the middle region and the low concentration contours have the same cusp-like shapes that extend more toward the stagnation point than in the other direction.

The intensity of the light passing through the cell is recorded by a charge coupled device camera and stored with a resolution 1 pixel per 20×20 $(\mu\text{m})^2$ for an area covering the central region of the returned tracer profile. The concentration field, being logarithmically related to the intensity, is obtained from this signal.

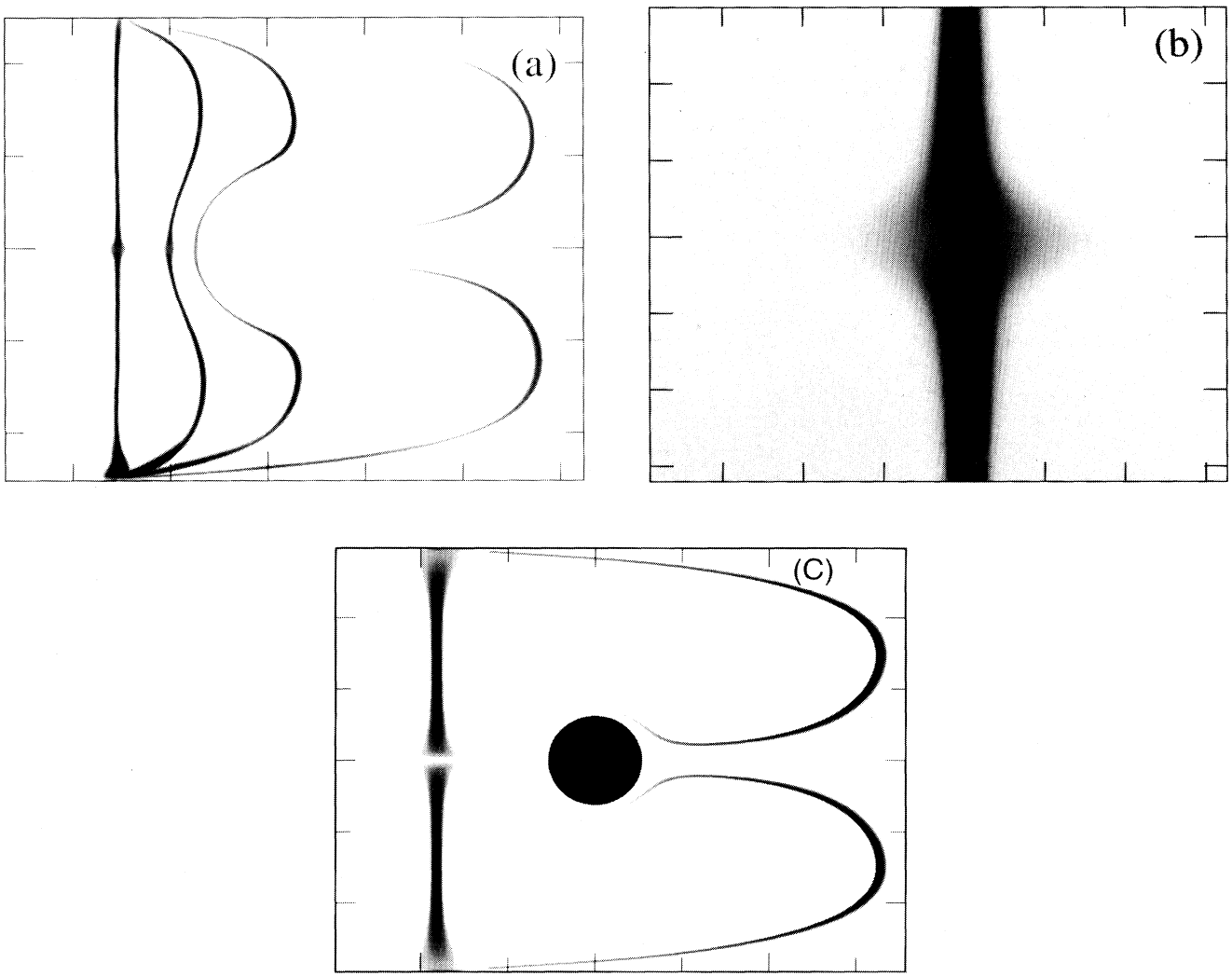

FIG. 2. (a) Four snapshots (from above) of the tracer line during return flow. Time increases going from right to left. The cylinder does not show since this is a difference image. The Reynolds number Re is 3.6×10^{-3}, the Péclet number Pe is 4×10^{5}, and the molecular diffusion coefficient $D\approx0.26\times10^{-7}$ cm^2/s. The grid mark spacing is 1 cm. (b) An enlargement of the characteristic mid-channel dispersion of the tracer line "echo." The grid mark spacing is 0.1 cm. (c) A corresponding plot of dispersion obtained in lattice Boltzmann simulations with Pe=2.2×10^{4}, shown at the instant of reversal and when the tracer has returned. The gray scale $\text{gr}(\mathbf{x})=\exp[-4C(\mathbf{x})]$, where gr =0 (gr =1) corresponds to black (white). The grid mark spacing is 177 lattice units.

III. BOLTZMANN MODEL

The particular lattice Boltzmann model used is known as a lattice Bhatnagar-Gross-Krook model. It is described in detail in the references [2,10]. It models the fluid as a large number of particles that move with unit velocities from site to site on a triangular lattice and interact by collisions conserving mass and momentum [11]. The basic variables are the probabilities $N_i(\boldsymbol{x},t)$ of finding a particle on a site at position $\boldsymbol{x}$ at time t moving with unit velocity in one of the six lattice directions labeled i and the probability Δ_i of that particle being a tracer particle. These probabilities are updated according to the scheme

$$N_i(\boldsymbol{x}+\boldsymbol{c}_i,t+1) = N_i(\boldsymbol{x},t) + \lambda_\nu \left[N_i(\boldsymbol{x},t) - N_i^{\mathrm{eq}}(\boldsymbol{x},t) \right] + \frac{1}{3}\boldsymbol{c}_i \cdot (\rho \boldsymbol{g}), \tag{2}$$

$$\Delta_i(\boldsymbol{x}+\boldsymbol{c}_i,t+1) = \Delta_i(\boldsymbol{x},t) + \lambda_D \left[\Delta_i(\boldsymbol{x},t) - \Delta_i^{\mathrm{eq}}(\boldsymbol{x},t) \right], \tag{3}$$

where λ_ν and λ_D are relaxation parameters that determine the kinematic viscosity ν and the molecular diffusion coefficient D, respectively. The equilibrium distributions are given as

$$N_i^{\mathrm{eq}} = (\rho/6)\,(1 + 2\boldsymbol{u}\cdot\boldsymbol{c}_i + 4GQ_{i\alpha\beta}u_\alpha u_\beta)\,, \tag{4}$$

$$\Delta_i^{\mathrm{eq}} = (C/6)\,(1 + 2\boldsymbol{u}\cdot\boldsymbol{c}_i)\,, \tag{5}$$

where $\boldsymbol{c}_i$ are the unit vectors connecting neighboring nodes on the lattice and

$$Q_{i\alpha\beta} = c_{i\alpha}c_{i\beta} - (1/2)\delta_{\alpha\beta}, \tag{6}$$

$\delta_{\alpha\beta}$ is the Kronecker delta function, and α and β are Cartesian indices. The mass density per site is defined as

$$\rho = \sum_i N_i\,, \tag{7}$$

the momentum density as

$$\rho\boldsymbol{u} = \sum_i \boldsymbol{c}_i N_i, \tag{8}$$

and the concentration as

$$C = \sum_i \Delta_i\ . \tag{9}$$

The quantities ρ, $\rho\boldsymbol{u}$, and C are conserved due to the choice of the equilibrium distributions. The last term of Eq. (2) is a forcing term giving a momentum input $\boldsymbol{g}$ per site per time step and G will reappear as a prefactor of the nonlinear term of the Navier-Stokes equation; see Eq. (11).

Equations (2) and (3) describe the two steps of the algorithm. First the probabilities undergo a local interaction according to λ_ν, λ_D and the site values of the conserved quantities and then they are propagated to the six neighboring sites according to their direction i. At boundary sites the probabilities are propagated back into the directions from which they came. This gives a no-slip boundary condition on $\boldsymbol{u}$.

It should be noted from Eqs. (2)–(9) that the time evolution of the N_i's is explicitly independent of the time evolution of the Δ_i's. This ensures that the hydrodynamic behavior of the model is independent of the diffusive behavior.

It can be shown [2,9] that the conserved quantities ρ, $\rho\boldsymbol{u}$, and C satisfy the equations of motion

$$\boldsymbol{\nabla}\cdot\boldsymbol{u} = 0, \tag{10}$$

$$\partial_t\boldsymbol{u} + G(\boldsymbol{u}\cdot\boldsymbol{\nabla})\boldsymbol{u} = -\frac{1}{\rho}\boldsymbol{\nabla}P + \nu\,\nabla^2\boldsymbol{u} + \boldsymbol{g}, \tag{11}$$

$$\partial_t C + (\boldsymbol{u}\cdot\boldsymbol{\nabla})C = D\,\nabla^2 C\,. \tag{12}$$

Equations (10) and (11) are the equations of incompressible hydrodynamics. Their validity is restricted by the incompressibility condition that the flow velocity $\boldsymbol{u}$ be small compared to the velocity of sound, i.e., that the Mach number be small [9]. In this case the dynamic modes with a rapid time dependence (like sound waves) will be suppressed with time, leaving only the slower processes as diffusion of momentum and tracer particles. The pressure P is given as $P = (1/2)\rho(1 - Gu^2)$. The velocity dependence in this expression results from the discreteness of the particle velocities: In general a flow velocity u is set up by ordering the directions of the particles into the direction of u. As a result, the probability of finding particles moving in the transverse direction is decreased. This corresponds to a drop in the pressure. In the case when $G = 0$, a flow velocity u results from an increase in the forward populations (with respect to u) and a decrease in the backward populations only and there is no decrease in the transverse populations. Correspondingly, P has no u dependence in this case. When $G = 1$ Eqs. (10) and (11) are simply the incompressible Navier-Stokes equations with a forcing term $\boldsymbol{g}$. The kinematic viscosity ν and the diffusion coefficient D are given by the relaxation parameters through the relations

$$\nu = -\frac{1}{4}\left(\frac{1}{\lambda_\nu} + \frac{1}{2}\right), \tag{13}$$

$$D = -\frac{1}{2}\left(\frac{1}{\lambda_D} + \frac{1}{2}\right)\ . \tag{14}$$

Equations (10)–(12) were derived by a Chapman Enskog expansion [9] in the gradients of the conserved quantities.

A. Viscous drag from the top and bottom plates of the Hele-Shaw cell

We want to model the flow in the central layer between the top and bottom plates of the Hele-Shaw cell since this

is where the tracer is located. In order to make the proper modification to Eqs. (2) and (3) we derive an equation of motion that describes the two-dimensional flow field $\boldsymbol{u}$ in this central layer. The full flow field $\boldsymbol{u}_{3D}$ in the Hele-Shaw cell is given by the three-dimensional Navier-Stokes equation

$$\partial_t \boldsymbol{u}_{3D} + (\boldsymbol{u}_{3D} \cdot \boldsymbol{\nabla})\boldsymbol{u}_{3D} = -\frac{1}{\rho}\nabla P + \nu \boldsymbol{\nabla}^2 \boldsymbol{u}_{3D} + \boldsymbol{g} \ . \quad (15)$$

Although there is no body force $\rho \boldsymbol{g}$ acting in the flow direction in the experiment, we include it here to make contact with the equations describing the model. By making the approximation that $\boldsymbol{u}_{3D}$ is parallel to $\boldsymbol{u}$ along any line in the z direction we can define a function f relating the full flow field to the one in the central layer ($z = 0$) through the relation

$$\boldsymbol{u}_{3D}(x, y, z, t) = f(x, y, z)\boldsymbol{u}(x, y, t) \ . \quad (16)$$

For the present purposes we neglect the possible time dependence in f. Inserting Eq. (16) into Eq. (15) and using the fact that by definition $f(x, y, 0, t) = 1$ and thus $\partial_x f(x, y, 0, t) = \partial_y f(x, y, 0, t) = 0$, we obtain the equation of motion for $\boldsymbol{u}$

$$\partial_t \boldsymbol{u} + (\boldsymbol{u} \cdot \boldsymbol{\nabla})\boldsymbol{u} = -\frac{1}{\rho}\boldsymbol{\nabla} P + \nu \boldsymbol{\nabla}^2 \boldsymbol{u} + \rho \boldsymbol{g} + \nu \boldsymbol{u} \partial_z^2 f, \quad (17)$$

which is similar to Eq. (11) except for the last term, which describes the viscous coupling to the top and bottom plates. In general $\partial_z^2 f$ will be a function of x, y, and t. However, far from the sidewalls in a Hele-Shaw cell f is well approximated by the parabolic function $p(z) = [1 - (2z/h)^2]$. Substituting p for f in Eq. (17) we get the equation

$$\partial_t \boldsymbol{u} + (\boldsymbol{u} \cdot \boldsymbol{\nabla})\boldsymbol{u} = -\frac{1}{\rho}\boldsymbol{\nabla} P + \nu \boldsymbol{\nabla}^2 \boldsymbol{u} + \left(\rho \boldsymbol{g} - \frac{8\nu}{h^2}\boldsymbol{u}\right) \ . \quad (18)$$

With the above approximations, the effect of the viscous drag from the top and bottom plates is described solely through the modification of the forcing term

$$\boldsymbol{g} \to \boldsymbol{g} - \frac{\nu}{8h^2}\boldsymbol{u} \ . \quad (19)$$

Making this substitution in Eq. (2) a new description of the model's dynamics given by the equation

$$\partial_t \boldsymbol{u} + G(\boldsymbol{u} \cdot \boldsymbol{\nabla})\boldsymbol{u} = -\frac{1}{\rho}\boldsymbol{\nabla} P + \nu \boldsymbol{\nabla}^2 \boldsymbol{u} + \left(\boldsymbol{g} - \frac{8\nu}{h^2}\boldsymbol{u}\right) \quad (20)$$

is obtained.

Two questions are now in order. How well does Eq. (20) approximate the exact equation of motion (15) and how well does the solutions obtained from simulations approximate the solutions of Eq. (17)? To give a partial answer to these questions we consider the flow with no-slip boundary conditions in a rectangular channel without obstacles for which the analytic solution is known.

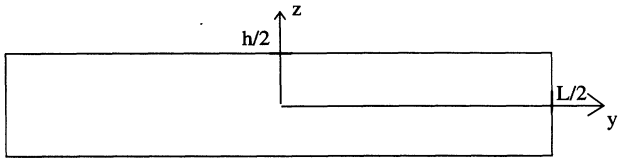

FIG. 3. Rectangular channel without obstacles. The flow is in the direction into the paper plane.

The flow u occurs in the geometry shown in Fig. 3 and the solution of Eq. (15) is given by [15]

$$u(y, z) = \frac{g}{8\nu}W^2\left\{\frac{1}{2}\left[1 - \left(\frac{y}{W/2}\right)^2\right] + \sum_{n=1,3,\ldots} A_n \cosh\left(\frac{n\pi}{W}z\right)\cos\left(\frac{n\pi}{W}y\right)\right\}, \quad (21)$$

where

$$A_n = -\frac{16}{\pi^3 n^3}\frac{(-1)^{(1/2)(n-1)}}{\cosh\left(\frac{n\pi h}{2W}\right)} \ . \quad (22)$$

If the ratio h/W is small the z dependence of u will be almost parabolic except close to the sidewalls (with height h). To get an estimate of the error made by the replacement of f by p in Eq. (17) we define

$$Q = (\partial_z^2 f)/(\partial_z^2 p) \ , \quad (23)$$

where f is obtained from Eqs. (21) and (16). Q is the ratio between the exact value of the last term of Eq. (17) and the approximation to this term.

Figure 4 shows Q as a function of the distance from a sidewall in units of h. It is seen that at $y = h/2$ the ratio Q equals unity within 7%. Hence the boundary layer

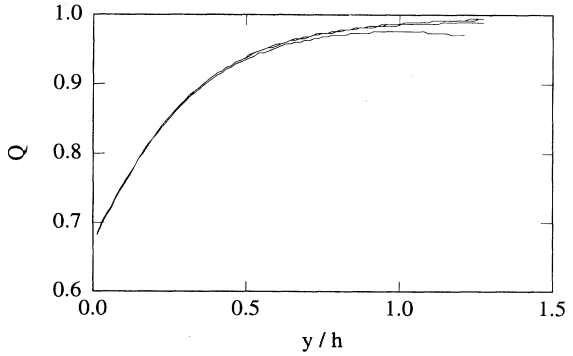

FIG. 4. Ratio $Q = \partial_z^2 f(\boldsymbol{x})/\partial_z^2 p(z)$ computed where $p(z)$ is a parabola shown at $z = 0$ as a function of the distance y from the wall in units of the channel height h. In fact, five curves corresponding to the height to width ratios $h/W = 0.1$, 0.2, 0.3, 0.4, and 0.5 are shown.

along the sidewall, where the z dependence significantly departs from parabolic, is thin and not very pronounced.

Figure 5 shows the flow velocity across the channel obtained from Eq. (21) and from simulations in which the replacement Eq. (19) is used. The deviations between simulations and the prediction of Eq. (21) are as expected: Very close to the sidewall the velocity profile of Eq. (21) will be quite flat in the z direction. The viscous drag from the top and bottom walls given by the term $|\nu\partial_z^2 f|$ will thus be smaller than $|\nu\partial_z^2 p|$, which is the term corresponding to the simulations. The effective forcing, given by $g - |\nu\partial_z^2 p|$, will therefore be smaller in the simulations than in a real system. In other words, the simulations will tend to overestimate the viscous interaction with the top and bottom walls close to the sidewalls. This is true also in more complicated geometries.

B. Reynolds and Péclet number

A basis for comparison between the synthetic world of the simulations and the real world of the experiments should be formed by describing the systems by dimensionless variables. The variables we will use are, in addition to the length ratios defining the geometry, the Reynolds and Péclet numbers. In the following we review the motivation for their definition [9,16]. In Sec. IV we will also introduce the dimensionless ratio D_{disp}/D, which we propose as the relevant quantity for the determination of the experimental value of D.

By defining the typical length and time scales d and $T = d/U$, where U is the average flow velocity in the three-dimensional channel and d the cylinder diameter, we can write the equations of motion (10)–(12) in terms of the dimensionless variables $x' = x/d$, $t' = t/T$, $\boldsymbol{u}' = \boldsymbol{u}/U$, $\overline{P}' = \overline{P}/(G\rho U^2)$, $C' = C/C_0$, and $\rho' = \rho/\rho_0$, where C_0 is some reference concentration, say, the maximum initial concentration and ρ_0 the average density.

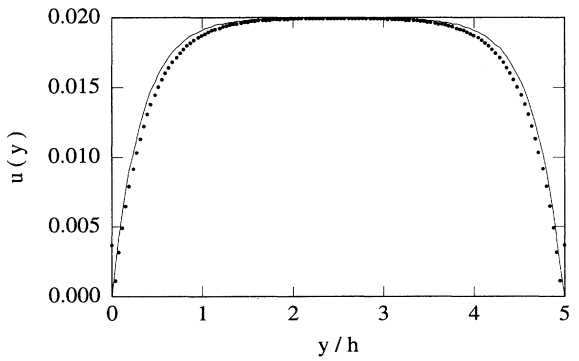

FIG. 5. Flow velocity $u(y)$ as a function of y/h, where h is the channel height in the z direction. Dots show results from simulation on a 128 × 128 lattice and the full line shows the analytic prediction given in Eq. (21) for $z = 0$. The height to width ratio is 0.20, the forcing $g = 8.3 \times 10^{-5}$, the viscosity $\nu = 0.25$, and the density $\rho = 3.0$.

[The fluid in the experiment is incompressible to an excellent approximation. The density in the simulations, however, exhibits variations of the order 1%. This variation is reflected in the equations of motion (10)–(12) through the ∇P term. The model thus satisfies the incompressibility condition only to a certain approximation [9].] We have absorbed the forcing term $\rho\boldsymbol{g}$ into $\overline{P} = P - \rho\boldsymbol{x}\cdot\boldsymbol{g}$. Since there is no body force applied in the experiment $\overline{P}$ corresponds to the experimental pressure. In these new variables Eqs. (10), (12), and (18) take the form

$$\nabla' \cdot \boldsymbol{u}' = 0, \tag{24}$$

$$\frac{1}{G}\partial_{t'}\boldsymbol{u}' + (\boldsymbol{u}'\cdot\nabla')\boldsymbol{u}' = -\frac{1}{\rho'}\nabla\overline{P}' + \frac{1}{\mathrm{Re}}\left(\nabla'^2\boldsymbol{u}' - \frac{8}{h'^2}\boldsymbol{u}'\right), \tag{25}$$

$$\partial_{t'}C' + (\boldsymbol{u}'\cdot\nabla')C' = \frac{1}{\mathrm{Pe}}\nabla'^2 C', \tag{26}$$

where the Reynolds and Péclet numbers are defined as

$$\mathrm{Re} = G\frac{Ud}{\nu}, \tag{27}$$

$$\mathrm{Pe} = \frac{Ud}{D}, \tag{28}$$

respectively. In the special case of steady state flow, which is the case in the experiment, the first term of Eq. (25) vanishes and the G dependence is through Re only. Equations (24)–(26) constitute five scalar equations for the five unknowns $\boldsymbol{u}'$, $\overline{P}'$, and C'. If the dimensionless numbers Re, Pe, and h' are the same for the simulations and the experiment they are described by the same equations and the same dimensionless flow field and concentration field will result, provided the model is in fact described by Eqs. (10), (12), and (18). The Reynolds number describing the experiment is defined without the G factor.

For the LGA the presence of a density-dependent G factor is generally considered a shortcoming of the models since it destroys the Galilean invariance of the fluid dynamic equations [17]. In the present context, however, it is a free parameter that can be used to tune the Reynolds number independently of the flow velocity, viscosity, and length scale. The ability to freely tune the Reynolds number of the simulations to the experimental value greatly reduces the computation time since the flow velocity can be increased (up to the limit set by the condition that the Mach number be small) and the time needed for the tracer to traverse the system decreased.

IV. LINEAR AND NONLINEAR DISPERSION

In the following we derive a result on simple diffusion to motivate the definition of the dispersion coefficient and we interpret the echo dispersion in terms of a time-of-arrival distribution $T(\mathbf{x})$. This is used to derive a condition on Pe to distinguish between the regime where the mean square spread of the tracer in the x direction, $\sigma^2(y)$, has a simple linear dependence on D and

the regime where the D dependence is nonlinear.

The one-dimensional diffusion equation

$$\partial_t C(x,y,t) = D\partial_x^2 C(x,y,t) \tag{29}$$

describes the time development of the initial concentration $C(x,y,0)$ given in Eq. (1) in the absence of flow. Referring to the experiment $C(x,y,t)$ is the projection of the concentration into the xy plane and has the dimension $1/l^2$, where l denotes length. With an arbitrary initial condition $C(x,y,0)$ Eq. (29) has the solution

$$C(x,y,t) = \frac{1}{\sqrt{4\pi Dt}} \int dx'\, C(x,y,0) \exp\left(-\frac{(x-x')^2}{4Dt}\right) . \tag{30}$$

Defining the conserved quantity $C_{\rm tot} = \int_{-\infty}^{\infty} dx\, C(x,y,0)$, $\sigma^2(y)$ takes the form

$$\begin{aligned}
\sigma^2(y) &= \frac{1}{C_{\rm tot}} \int_{-\infty}^{\infty} dx\, (x-x_0)^2 C(x,y,t) \\
&= \frac{1}{C_{\rm tot}} \int_{-\infty}^{\infty} dx\, dx'\, (x-x_0)^2 \\
&\quad \times \frac{1}{\sqrt{4\pi Dt}} \exp\left(-\frac{(x-x')^2}{4Dt}\right) C(x',y,0) \\
&= \frac{1}{C_{\rm tot}} \int_{-\infty}^{\infty} dx\, dx'\, (x+x'-x_0)^2 \\
&\quad \times \frac{1}{\sqrt{4\pi Dt}} \exp\left(-\frac{x^2}{4Dt}\right) C(x',y,0) \\
&= \frac{1}{C_{\rm tot}} \left(2Dt \int_{-\infty}^{\infty} dx'\, C(x',y,0) \right. \\
&\quad \left. + \int_{-\infty}^{\infty} dx'\, (x'-x_0)^2 C(x',y,0) \right) \\
&= 2Dt + \sigma^2(t=0)
\end{aligned} \tag{31}$$

where, in passing from the second to third line above, the substitution $x \to x + x'$ was used. In passing from the third to fourth line, we used that the integral of the cross terms in x and x' vanish.

It follows that for arbitrary $C(x,y,0)$ the change in $\sigma(y)$ in an interval Δt is

$$\Delta\sigma^2(y) = 2D\Delta t. \tag{32}$$

Solving for D we obtain the expression for the effective diffusion constant

$$D_{\rm disp} = D = \frac{\Delta\sigma^2(y)}{2\Delta t} . \tag{33}$$

This is the expression for $D_{\rm disp}$ that we will apply to the dispersed profile, in which case Δt will be the time of return of the tracer line and x_0 the maximum point of $C(x,y,t)$ along the constant-y line. When there is no flow $D_{\rm disp} = D$. When there is a flow, $D_{\rm disp}$ and D will generally differ strongly. Note that, for the purpose of comparing the quantity $D_{\rm disp}$ from simulations and experiments, there is no need to use the same x dependence in the initial concentration profiles $C(x,y,0)$.

For each streamline we shall denote by B the position of reversal and by C the final position of a fluid particle and we shall consider the effect of a displacement $\boldsymbol{\sigma}_B$ at the position of reversal, on the final position of the particle, given by the displacement $\boldsymbol{\sigma}_C$ relative to the initial position. Consider the convective transport time $T(\mathbf{x})$, which for a given x_0 and U is the time it takes for a particle to arrive by convection alone at $\mathbf{x}$ from the initial line $x = x_0$. T will diverge where the velocity vanishes, in particular at the surface of the cylinder, where $r \equiv |\mathbf{x}| = r_0$. When $|x_0|$ is sufficiently large, the streamlines are approximately parallel to the walls and the velocity approximately constant in the x direction. Hence the displacement $\sigma_C(y)$ is given, to a good approximation, as $\sigma_C(y) = u_{x_0}(y)\Delta T$, where

$$\Delta T(\mathbf{x}) = T(\mathbf{x} + \boldsymbol{\sigma}_B) - T(\mathbf{x}) . \tag{34}$$

Since the field T can, in principle, be obtained by the integration of a differentiable velocity field, it is itself differentiable and we can Taylor expand Eq. (34) as

$$\Delta T(\mathbf{x}) = \boldsymbol{\sigma}_B \cdot \boldsymbol{\nabla} T(\mathbf{x}) + \frac{1}{2}(\boldsymbol{\sigma}_B \cdot \boldsymbol{\nabla})^2 T(\mathbf{x}) + \cdots . \tag{35}$$

The dispersive spread $\sigma^2(y)$ is obtained by taking the square of Eq. (35) and averaging the resulting terms with the aid of the probability distribution of the $\boldsymbol{\sigma}_B$'s that corresponds to ordinary, isotropic diffusion. For the second moment this will give $\langle \sigma_B^2 \rangle \approx 2Dt_c$, where t_c is some characteristic time over which the diffusion takes place, say, d/U. Hence, for σ^2 to be linearly related to D the first term must dominate the right-hand side of Eq. (35). In the following we examine the condition for this to be the case. Corresponding to the fact that a displacement $\boldsymbol{\sigma}_B$ *across* streamlines will cause a much larger $\sigma_C(y)$ than a displacement *along* streamlines, $\nabla T \approx \mathbf{u}_r\, \partial T/\partial r$, where $\mathbf{u}_r$ is the unit vector in the radial direction from the cylinder center.

Making the assumption that, for small $r - r_0$, the time of arrival distribution has the form

$$T(\mathbf{x}) = \frac{A_\Theta}{(r-r_0)^{\gamma_\Theta}} , \tag{36}$$

where the angle Θ is measured from the positive x axis and the exponent γ_Θ may depend on this angle, we obtain the ratio between the first and second terms of Eq. (35) in the simple form

$$\left| \frac{(\boldsymbol{\sigma}_B \cdot \boldsymbol{\nabla})^2 T(\mathbf{x})}{\boldsymbol{\sigma}_B \cdot \boldsymbol{\nabla} T(\mathbf{x})} \right| = (\gamma_\Theta + 1) \frac{|\boldsymbol{\sigma}_B \cdot \mathbf{u}_r|}{(r-r_0)} . \tag{37}$$

The condition that $\Delta\sigma^2(y)$ be linear in D then takes the form

$$|\boldsymbol{\sigma}_B \cdot \mathbf{u}_r| \ll \frac{2(r-r_0)}{(\gamma_\Theta + 1)} . \tag{38}$$

If we estimate the radial diffusive displacement $|\boldsymbol{\sigma}_B \cdot \mathbf{u}_r|$ by the diffusive length $l_D = \sqrt{Dd/U}$, Eq. (38) becomes

$$l_D \ll \frac{2(r-r_0)}{\gamma_\Theta + 1} , \tag{39}$$

which can be rewritten as a condition on the Péclet number $\mathrm{Pe} = (d/l_D)^2$,

$$\sqrt{\mathrm{Pe}} \gg (\gamma_\Theta + 1)\frac{r_0}{r - r_0} . \tag{40}$$

When the condition Eq. (39) is not fulfilled, the dispersion $\Delta\sigma^2(y)$ will in general have a nonlinear D dependence. For every value of $x_{\max}$, this condition may therefore serve to distinguish between the high and low Péclet number regimes. In the high Pe regime results can be extrapolated to higher or lower Pe by the use of the linearity of σ^2 in D. However, in the low Pe regime no simple extrapolation scheme seems to exist. For the experiments and the simulations, performed on a 512×1024 lattice, the relevant Péclet numbers are given by

$$\sqrt{\mathrm{Pe}} = \begin{cases} \sqrt{400\,000} = 632 & \text{in experiment} \\ \sqrt{22\,365} = 150 & \text{in simulation.} \end{cases} \tag{41}$$

When we use $r - r_0 \approx r_0/10$ as is the case when $x_{\max} = 6\ r_0$ and take $\gamma_\Theta = 1$, the right-hand side of Eq. (40) takes the (characteristic) value 22. The estimate of γ_Θ follows from the assumption that close to the stagnation point the velocity decays as the square of the distance to the stagnation point, as in the case of a free cylinder. It seems reasonable to assume that the experiment is well within the high Péclet number regime, whereas the simulations are on or close to the border of this regime.

V. SIMULATIONS AND THE EXPERIMENTS

Before we turn to the comparison between the simulations and experiments, we discuss the technical aspects of the two. In the experiment (see Fig. 1) a thin straight filament of a mixture of 90% glycerol and 10% water dyed with 0.2% nigrosine was injected by a syringe in the middle between the glass plates of a Hele-Shaw cell filled with a mixture of 90% glycerol and 10% water. The viscosity of this mixture was $\mu \simeq 400$ cP; the dyed fluid had a viscosity that was 2–3% lower. The effect of the viscosity contrast appears to be negligible. The density of the two fluids was $\rho = 1.2318 \pm 0.0001$ g/cm^3. It is critical for the success of the experiment that the densities are well matched. The molecular diffusion constant D was measured independently by simply letting the tracer diffuse without flow. Equation (33) then gives the value

$$D = (0.28 \pm 0.02) \times 10^{-7}\ \mathrm{cm}^2 . \tag{42}$$

This result will be compared with the value of D obtained from measuring the dispersion of the reversed profile. The experimental apparatus is similar to that used by Hiby [18] in his study of dispersion and reversibility of viscous flow in random media. The flow is started abruptly after the dye is injected. It then takes some time for the flow to reach steady state. This relaxation time can be (over)estimated as $t_{\mathrm{rel}} = W^2/(\pi^2\nu)$, where W is the channel width and ν the kinematic viscosity. The time t_{rel} is the characteristic time it takes for the flow field in a two-dimensional channel of width W to reach steady state. In the experiment t_{rel} is less than 1 s whereas the total flow time is more than 100 s. The experiment was controlled by visual inspection both to reverse the flow at the point maximum displacement $x_{\max}$ and to stop the flow when the tracer has returned to the initial position. The experimental error in determining the positions was ± 1 mm, i.e., $\pm 0.2 r_0$. The simulation is stopped when the point of maximum concentration along the line $y = W/4$ has returned to x_0.

Using Eq. (33) to determine the experimental values of D_{disp} is not as straightforward as one might think [1]. The tracer fluid is injected in the Hele-Shaw cell by hand and the values of a will vary with y. As the tracer is injected, the syringe will create a slight disturbance in the fluid and cause a slight initial dispersive mixing. As a result there will be a dispersive mixing prior to the initialization of the overall flow and the initial concentration profile will not simply be given by Eq. (1). It follows that the initial mean square spread $\sigma^2(y)$ given by Eq. (33) will be larger than $a^2/4$, which is the mean square width of cylindrical profile. In the experiment the initial value of $\sigma^2(y)$ is measured in order to obtain $\Delta\sigma^2(y)$ after a time Δt.

Figure 2(c) shows the simulated concentration field when the flow is reversed and when the tracer has returned. Figure 2(b) shows the corresponding central part of the experimental (returned) concentration profile. Figure 6 shows the (returned) concentration profiles in sections in the x direction corresponding to Fig. 2(c). The Péclet number for the simulation was 2.2364×10^4 and for the experiment it was 4×10^5. The symmetry of the problem was used to perform the simulations on the upper half of the system only. The picture in Fig. 2(c) was obtained from a simulation on a 512×1024 lattice. Since the boundary conditions were periodic in the direction of the flow, a piece of the rightmost lobes reenter on the left-hand side of the lattice. This has been corrected for by pasting this leftmost part of the picture onto the rightmost side, thus giving an aspect ratio of the picture that is slightly larger than that corresponding to a square portion of a triangular lattice.

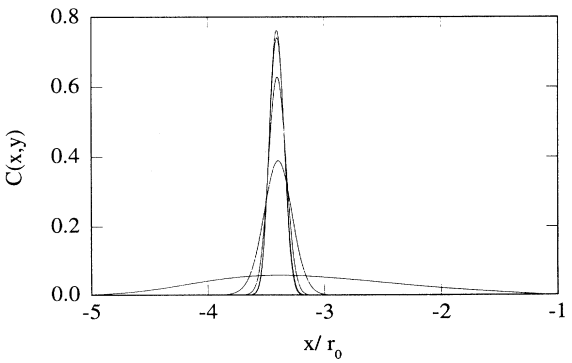

FIG. 6. Concentration profiles in the x direction corresponding to Fig. 2. The subsections are taken at $y = 0$, $W/16$, $W/8$, $3W/16$, and $W/4$. The $y = 3L/16$ and $W/4$ curves fall on top of each other.

In order to keep the simulations within the limits where the model is numerically stable and well described by theory, $\nabla C/C$ must be relatively small. However, as shown in Ref. [2], the model remains quite well behaved even when $\nabla C/C \approx 0.5$. In the experiment the initial width of the tracer must be sufficiently small to ensure that dispersive effects due to the variations of the flow velocity in the z direction does not dominate. The simulation value $r_0/a = 6.6$ results from the values $r_0 = 87$ and $a = 13$ lattice units. Since $\nabla C/C \sim 1/a$, the initial profile is well within the regime where the model behaves physically. For reasons of numerical stability the Péclet number of the simulations cannot be made significantly larger than the above value. In the experiment the Péclet number cannot be made significantly smaller than the above value. The reasons for this is mainly that the tracer, if convected to slowly, moves out of the central plane and the returned signal becomes distorted.

Since the flow was steady, the simulations were carried out in two steps, one giving the velocity field and one giving the dispersion. In the first step, the lattice was initialized with zero flow velocity everywhere. Then the forcing was applied and the flow allowed to reach steady state. In the second step computer memory and CPU time was saved by only updating the Δ_i's. The reversed flow field was obtained by the simple substitution $\mathbf{u} \to -\mathbf{u}$. The linearity of the Stokes equations allows for a global rescaling of the velocity so that the maximum value was $u_{\max} = 0.1$. This was done as another means to reduce computation time and to increase the Péclet number as far as possible. On a 128 node Connection Machine (CM5) computer the code that only updates the Δ_i's ran at $(8\text{–}9)\times 10^6$ site updates per second— a speed that in practice allows overnight simulations on 2048×1024 lattices to be carried out.

The molecular diffusion coefficient $D = 5 \times 10^{-4}$ and the initial mass density is $\rho = 3.0$. The forcing used to initiate the flow was $g = 1.80 \times 10^{-5}$, the viscosity $\nu = 1.0$, and the resulting maximum flow velocity before rescaling is 0.023 lattice units per time step. The maximum value of the concentration in the initial profile is $C_{\max} = 1.0$. The maximum distance past the center of the cylinder reached by the tracer $x_{\max} = 6.0r$. The Reynolds number of the simulation was set to zero in accord with the very small Reynolds number of the experiment Re$= 3.6 \times 10^{-3}$.

As can be seen from Fig. 6, which shows sections of the concentration profile in the x direction for various values of y, the concentration $C(x, y, t)$ exhibits an asymmetry in the middle of the channel. This reflects the steepness of the velocity gradient near the stagnation points, which causes the diffusive spread σ_B in the direction of the stagnation point to result in a larger dispersion than a spread in the opposite direction. In the simulation producing Fig. 2(c) the ratio $a/r = 1/6.6$, whereas in the experiment $a/r = 1/25$.

The simulations were also carried out without the viscous coupling to the top and bottom walls given by the last term of Eq. (19). This gave a different shape of the tracer line, especially at the instant of reversal of the flow where the lobes had a more stretched shape, being slightly more sharply curved at the rightmost side. As a consequence of this the minimum value of D_{disp} had the value $0.98D$, which is significantly larger than in the case where the viscous coupling to the top and bottom walls are included.

In the simulations, small regions in which the concentration oscillates between negative and positive values develop initially. This phenomenon is seen on the right-hand side of Fig. 2(c), where some thin tracer lines are seen to lag behind the main profile. These negative C "ripples" have small amplitude, they only occur when D is very small (below 10^{-4}), and they disappear as the flow progresses. This effect is also observed under similar circumstances in finite difference simulations [19] and is related to the numerical instability which sets in when D is too small.

VI. COMPARISON AND DISCUSSION

Figure 7 shows the experimental and simulated effective diffusion coefficients in units of D. The experimental and simulated values correspond to Figs. 2(b) and 2(c), respectively. The agreement between the two curves shown in Fig. 7 is very good in the region of significant dispersion. By choosing the experimental D that gives the best fit in this region the value

$$D = 0.26\ 10^{-7}\ \text{cm}^2/\text{s} \tag{43}$$

was obtained. This is in good agreement with the result obtained from independent measurements of the spread caused by diffusion alone.

The larger experimental than simulated values of D_{disp} for $|y|/r_0 > 0.1$ is as expected since no perturbation of the experiment can result in a reduction of the mixing. There are two such perturbations in particular: The finite ratio between the linewidth and channel height h will lead to dispersive effects due to the variation of the velocity field in the z direction. A slight vertical convective displacement of the tracer will have the same effect.

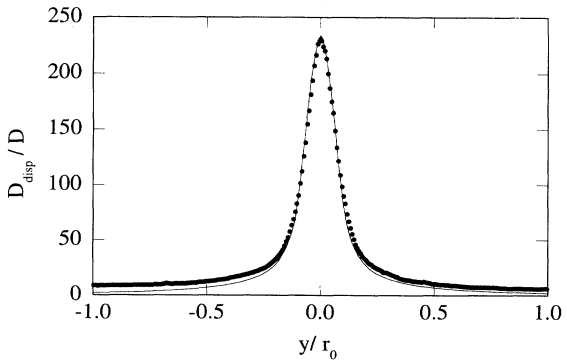

FIG. 7. Experimental (•) and simulated (full line) values of the dispersion coefficient, normalized by the diffusion coefficient D_{disp}/D, corresponding to the returned concentration profiles shown in Fig. 2 as functions of the position across the channel.

The tracer particles that have the range of positions $|y|/r_0 > 0.1$ upon return form a region that is wrapped around the cylinder at flow reversal. Hence the dispersed return profile represents a map of the hydrodynamic field around the entire cylinder and not only the local field at the stagnation point.

Figure 8 shows $\log_{10}(D_{\rm disp}/D)$ as a function of y. The fact that $D_{\rm disp}$ has a minimum value $0.80D$ that is *smaller* than D can be understood by the fact that the velocity gradients can cause both an increase and a decrease of the concentration gradients. In regions where the concentration gradient is decreased, the diffusive spread, and hence the final dispersion, will be reduced.

The magnitude of the dispersive effects of the stagnation point depends strongly on $x_{\rm max}$. This is shown in Fig. 9 where $\log_{10}[\max(D_{\rm disp}/D)]$ is shown for various values of $x_{\rm max}$. The simulations can easily handle the small values of $x_{\rm max}$, which in the experiment are challenging because of the limited resolution. The experiment, on the other hand, can easily deal with the cases of higher $x_{\rm max}$ values, where, in the simulations, new effects enter when the tracer diffuses all the way onto the cylinder wall.

We now comment upon a possible scaling interpretation of the results shown in Fig. 9. For the small values of $x_{\rm max}$ the dispersion stems from a flow field that is sensitive to all the length scales in the system. For the high values of $x_{\rm max}$ the simulations leave the high Péclet number regime (since $r - r_0$ becomes too small) and an increase in $x_{\rm max}$ will cause the nonlinearities in D to become important. In other words, the results depend on the length scale l_D, which no longer satisfies Eq. (39). However, in the intermediate regime where $D_{\rm disp}$ is a linear function of D and simulations and experiments are comparable, the dispersion is mainly sensitive to the length scale $r - r_0$. This length is given by some power of the time, which in turn is roughly linearly related to $x_{\rm max}$. Hence, in the regime of large $x_{\rm max}$ experiments and simulations should exhibit the same scaling behavior in $x_{\rm max}/r_0$, up to the cutoff defined by Eq. (39). In Fig. 9 the dashed curve shows a straight line fit to the experimental data and it is seen that the corresponding

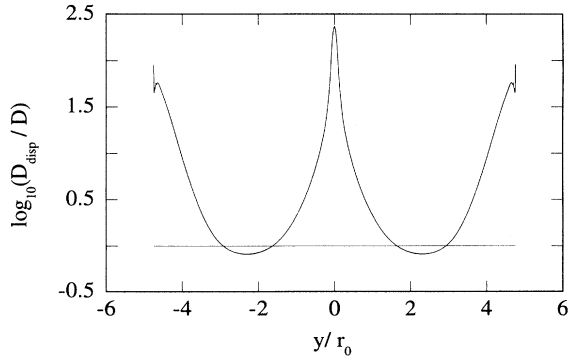

FIG. 8. Same simulated values of $D_{\rm disp}/D$ (where $D = 5 \times 10^{-4}$) as shown in Fig. 7, but here shown on a log-linear plot over the whole range of y. The straight line corresponds to $D_{\rm disp}/D = 1$.

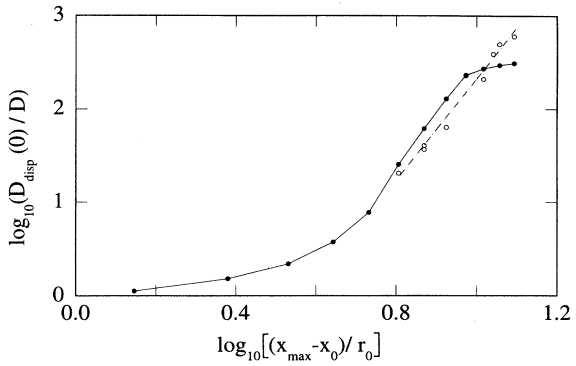

FIG. 9. Maximum effective diffusion constant $D_{\rm disp}(y = 0)/D_m$ as a function of the distance from the starting point $(x_{\rm max} - x_0)/r$, where $D = 0.26 \times 10^{-7}$ cm^2/s. •, simulations; ○, experimental results. The dashed line with a slope of 5.5 ± 0.4 is a fit to the experimental data.

slope 5.5 ± 0.4 is in agreement with the value 5.7, obtained from the straight part of the simulated curve.

In the case of geometric echo dispersion in porous media the averaged $\Delta\sigma^2$ scales linearly with the penetration depth [3], which is the length that corresponds to $x_{\rm max}$ in the present case. However, at sufficiently high Péclet numbers, in the sense given in Eq. (40), the dispersion will be dominated by the stagnation point effect and the scaling with the penetration depth will be different.

As seen from Fig. 8, $D_{\rm disp}(y)$ varies over more than two orders of magnitude. In the experiment the large values of $D_{\rm disp}$ corresponds to a diffusive spread of the tracer that is visible with the bare eye and thus gives a fairly accurate value of $D_{\rm disp}(y)$ from Eq. (33), whereas the smaller values of $D_{\rm disp}$ (which are of the order D) correspond to a spread that is much more difficult to measure. In the simulations, however, the molecular diffusion coefficient is known exactly as an input parameter and the values of $D_{\rm disp}$ can be measured with good accuracy. Consequently, by equating the ratios $D_{\rm disp}/D$ from the experiments and simulations, the unknown D for the experiments can be obtained.

It is in general difficult to determine molecular diffusion coefficients experimentally. A method developed by Taylor in 1953 [20] utilizes the enhancement of the mixing process by dispersion in a capillary tube at Pe$\ll 1$. The present experiment combined with the simulations constitutes an alternative method at high Péclet numbers. However, for the sake of measuring diffusion coefficients only, more practical geometries, such as the cylindrical Couette cell, can be employed.

VII. CONCLUSION

We have described a dispersion experiment in a Hele-Shaw cell that singles out the dispersion that occurs at stagnation points and we have related this type of dispersion to that which occurs in a random medium at lower Péclet numbers. We have in particular shown how the

dispersion scales with the maximum distance traversed by the tracer fluid.

On the theoretical side we have introduced an estimate of the Péclet numbers that distinguishes between the regimes where the dispersion is a linear and a nonlinear function of D. This might be useful for the purpose of distinguishing between different types of dispersion occurring in more complex geometries than the present one.

We have developed and analyzed a lattice Boltzmann model that is adapted to the experiment and compared results from simulations and experiment. As a test of the model we also demonstrated agreement between simulations and analytic results for the simple flow in a rectangular channel. By quantifying the observed dispersion by a dispersion coefficient (D_{disp}) we showed excellent agreement between the diffusive behavior of the model and the experiment. In this context it should be noted that the present application is a challenging one on account of the fact that the system is characterized by a wide variety of length scales: There is at least one order of magnitude between the overall size of the system W, the initial width of the tracer line a, and the smallest width of the tracer line upon reversal of the flow. In the simulations there was also a separation between these scales and the lattice constant.

The stagnation point dispersion is orders of magnitude higher than the spread that results from diffusion alone. This effect can be used as a means to measure very small diffusion coefficients D. In the present case we demonstrated that the values of D measured by dispersion agreed well with values obtained independently.

ACKNOWLEDGMENTS

We are grateful to T. Rage for valuable discussions and P. Meakin for helpful comments. We are also grateful to Jean Pierre Rivet for his critical remarks and helpful suggestions. We acknowledge support by VISTA (Grant No. 6311), a research cooperation between the Norwegian Academy of Science and Letters and Den Norske Stats Oljeselskap a.s. (STATOIL), by NFR, the Norwegian Research Council for Science and the Humanities Grant Nos. 100339/431, 100666/410, and 100198/410, and a grant from Norsk Hydro. Most of the computations were done on the Connection Machine (CM5) funded by the French Ministry of Education (MEN) and National Center for Scientific Research (CNRS).

[1] U. Oxaal, E. G. Flekkøy, and J. Feder, Phys. Rev. Lett. **72**, 3514 (1994).
[2] E. G. Flekkøy, Phys. Rev. E **47**, 4247 (1993).
[3] P. Rigord, A. Calvo, and J. Hulin, Phys. Fluids A **2**, 681 (1990).
[4] I. Ippolito, G. Daccord, E. J. Hinch, and J. P. Hulin, J. Cont. Hydr. **16**, 87 (1994).
[5] *Disorder and Mixing*, edited by E. Guyon, J.-P. Nadal, and Y. Pomeau (Kluwer, Dordrecht, 1988).
[6] *Hydrodynamics of Dispersed Media*, edited by J. P. Hulin, A. M. Cazabat, E. Guyon, and F. Carmona (North-Holland, Amsterdam, 1990).
[7] D. Koch and J. Brady, J. Fluid Mech. **154**, 399 (1985).
[8] C. Baudet, E. Guyon, and Y. Pomeau, J. Phys. (Paris) Lett. **46**, L991 (1985).
[9] *Lattice Gas Methods for Partial Differential Equations*, edited by G. D. Doolen (Addison-Wesley, New York, 1990).
[10] Y. H. Qian, D. d'Humières, and P. Lallemand, Europhys. Lett. **17**, 479 (1992).
[11] U. Frisch, B. Hasslacher, and Y. Pomeau, Phys. Rev. Lett. **56**, 1505 (1986).
[12] R. Holme and D. H. Rothman, J. Stat. Phys. **68**, 409 (1992).
[13] F. J. Higuera and S. Succi, Europhys. Lett. **8** (6), 517 (1989).
[14] D. H. Rothman, Phys. Rev. Lett. **65**, 3305 (1990).
[15] G. K. Batchelor, *An Introduction to Fluid Dynamics* (Cambridge University Press, Cambridge, 1970).
[16] D. J. Tritton, *Physical Fluid Dynamics* (Clarendon, Oxford, 1988).
[17] A. K. Gunstensen and D. H. Rothman, Physica D **47**, 47 (1991).
[18] J. W. Hiby, in *Symposium on the Interaction between Fluids and Particles*, edited by P. A. Rottenburg and N. T. Shepherd (The Institution of Chemical Engineers, London, 1962), pp. 312–325.
[19] H. P. Langtangen (private communication).
[20] G. I. Taylor, Proc. R. Soc. London Ser. A **219**, 186 (1953).

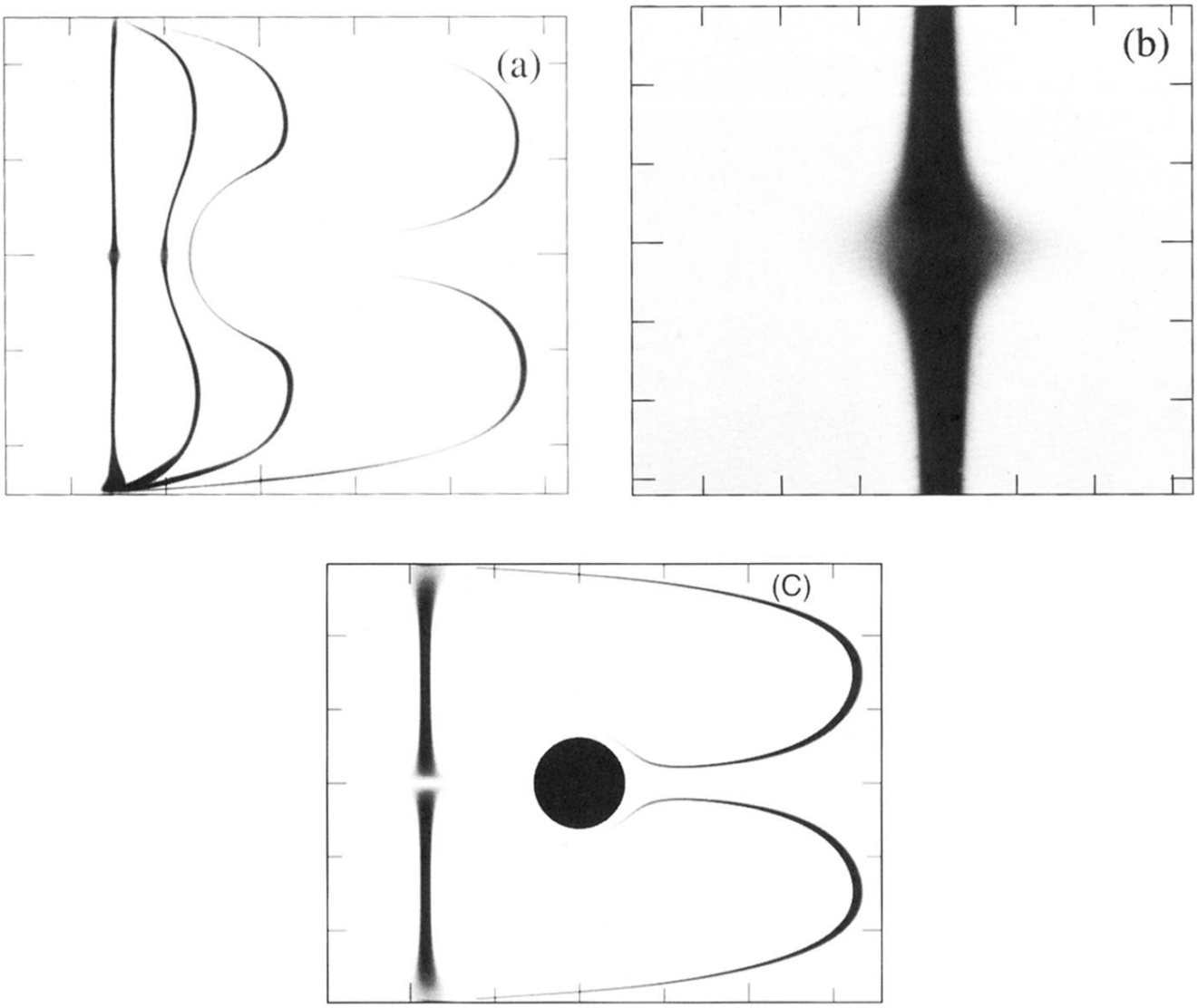

FIG. 2. (a) Four snapshots (from above) of the tracer line during return flow. Time increases going from right to left. The cylinder does not show since this is a difference image. The Reynolds number Re is 3.6×10^{-3}, the Péclet number Pe is 4×10^{5}, and the molecular diffusion coefficient $D \approx 0.26 \times 10^{-7}$ cm^2/s. The grid mark spacing is 1 cm. (b) An enlargement of the characteristic mid-channel dispersion of the tracer line "echo." The grid mark spacing is 0.1 cm. (c) A corresponding plot of dispersion obtained in lattice Boltzmann simulations with Pe=2.2×10^{4}, shown at the instant of reversal and when the tracer has returned. The gray scale $\mathrm{gr}(\mathbf{x}) = \exp[-4C(\mathbf{x})]$, where gr =0 (gr =1) corresponds to black (white). The grid mark spacing is 177 lattice units.